Available online at www.sciencedirect.com

ScienceDirect

Procedia Structural Integrity 80 (2026) 279–288

Structural Integrity Procedia

www.elsevier.com/locate/procedia

Fracture, Damage and Structural Health Monitoring

Numerical Methods for Thermo-Structural Analysis in Tubular Heat Exchanger Reactors for Synthetic Fuel Production

Saverio Giulio Barbieri[a,*], Andrea Piergiacomi[a], Matteo Giacopini[a], Fabio Ruggeri[b]

[a]*University of Modena and Reggio Emilia, Engineering Department "Enzo Ferrari", via Vivarelli 10, Modena (MO) 41125, Italy*
[b]*Synhelion AG, Dufourstrasse 101, Zürich 8008, Switzerland.*

Abstract

The transition to sustainable energy sources has intensified interest in synthetic fuel production, offering an alternative to fossil fuels. Tubular heat exchanger reactors play a critical role in this process, enabling efficient thermal exchange and chemical reactions under extreme operating conditions. However, these reactors face significant challenges related to thermal gradients, structural stresses, and long-term material degradation, requiring advanced numerical tools for accurate analyses. This study presents the development and application of numerical methods for the thermo-structural analysis of tubular heat exchanger reactors. A comprehensive approach was adopted to assess the thermal and mechanical behaviour of reactor components, incorporating material properties such as creep characteristics. Thermal simulations revealed significant temperature gradients across the reactor walls. Thermo-structural analyses were performed comparing two different materials, considering the effects of tensile loads, internal pressure, and creep phenomena. Special attention was given to the structural influence of the catalyst mass housed within the tubes. Additionally, different mounting strategies were evaluated. This work highlights the crucial role of advanced numerical modelling techniques in the design of efficient and durable tubular reactors, supporting the development of enhanced synthetic fuel production processes. Future work will focus on the detailed analysis of the manifold system and structural connections.

Keywords: Finite Element; thermo-structural analysis; creep; tubular heat exchanger reactors; synthetic fuel production.

* Corresponding author. Tel.: +39-059-205-6112.
E-mail address: saveriogiulio.barbieri@unimore.it

2452-3216
10.1016/j.prostr.2026.02.027

1. Introduction

The aviation sector accounted for approximately 2-3% of global CO_2 emissions in 2022, yet its impact on climate change is disproportionately high due to the additional effects of non-CO_2 emissions at high altitudes, such as nitrogen oxides (NO_x), water vapor, and contrail-induced cirrus clouds. As air traffic continues to grow, the need for drastic decarbonization within the industry is becoming increasingly urgent. In response, the European Union has set ambitious targets, including a 55% reduction in CO_2 emissions by 2030 and a goal of net-zero emissions by 2050, aligning with broader climate neutrality objectives (Baldino, 2023; Van Dyk and Saddler, 2024; Wang et al., 2024). Among the available solutions for sustainable aviation, synthetic fuels (also known as e-fuels) are emerging as a viable alternative to conventional jet fuels. Unlike electric propulsion, which is limited in aviation due to the high weight of batteries and their lower energy density compared to liquid fuels (Guiducci et al., 2023), synthetic fuels offer a direct drop-in replacement that can be used with existing aircraft engines and infrastructure. Produced from captured CO_2 and green hydrogen through power-to-liquid processes, these fuels have the potential to significantly reduce the carbon footprint of aviation when sourced from renewable energy (Grim et al., 2022; Piergiacomi et al., 2025; TotalEnergies and Airbus, 2024; Wolft and Riefer, 2020). Despite the promise of synthetic fuels, challenges remain, including high production costs and the need for large-scale renewable energy generation to make the process truly sustainable. However, continued advancements in technology and policy support are expected to drive down costs and increase production capacity in the coming years, making synthetic fuels a cornerstone of the green transition of the aviation sector.

This paper considers the production of synthetic gas via the “Sun-to-Liquid” process. This method harnesses concentrated solar energy to produce high-temperature process heat, which drives a thermochemical reactor to synthesize syngas, a mixture of hydrogen and carbon monoxide. The syngas is subsequently processed into liquid fuels such as jet fuel, gasoline, and diesel via standard gas-to-liquid technology (Awani et al., 2024; Ribun et al., 2023). The “Sun-to-Liquid” process integrates four key technological innovations. A field full of mirrors concentrates solar radiation onto a high-temperature receiver. A solar receiver converts concentrated radiation into process heat, exceeding 1500 °C, a temperature range rarely achieved in renewable fuel production and enabling efficient thermochemical conversion. A thermochemical reactor utilizes heat to drive endothermic reactions for syngas generation. Finally, a thermal energy storage system enables continuous, uninterrupted operation, effectively overcoming the intermittency of solar energy (Zavattoni et al., 2024, 2023, 2022, 2020). The integration of high-temperature solar thermochemistry with efficient energy storage represents a significant step toward a sustainable and scalable fuel solution for the aviation sector.

The tubes forming the core of tubular heat exchanger reactors are subjected to exceptionally high thermomechanical loads and must therefore be carefully designed (Gupta et al., 2022; Patil and Anand, 2017; Shafiee and McCay, 2016). The primary damage mechanisms include pure mechanical fatigue, creep, and corrosion. It is well known that these three contributions can be assessed using the Sehitoglu damage model (Su et al., 2002) or more comprehensive energy-based criteria (Charkaluk and Constantinescu, 2000; Lorenzini et al., 2023, 2018). In the present study, particular emphasis is placed on the dominant role of creep and the design parameters that may accelerate its effects. More specifically, the analysis focuses on two different materials, internal pressure, anchoring methods for the internal catalytic material, and the mounting configurations of the tubes.

The paper is structured as follows. First, the material properties relevant to high-temperature operation are described for two different materials, with particular emphasis on creep behaviour. A thermal analysis is then carried out to evaluate the heat transfer within a single reactor tube under operational conditions. This is followed by a series of preliminary thermal-mechanical analyses designed to isolate and understand the contribution of thermal loads, internal pressure, and axial tensile forces. Subsequently, creep behaviour is introduced into the model, and its effects are analysed for the two different materials, highlighting substantial performance differences. The impact of the catalyst material inside the tube is then investigated, with special attention to how its mass and support configuration influence the axial stress and structural response. The study then explores the influence of different tube mounting strategies, focusing on how mechanical constraints from manifold design affect deformation and stress distribution. Creep and non-creep cases are compared, and the performance of both materials is assessed under these boundary conditions. Finally, some conclusions end the manuscript.

2. Material properties

In this study, two materials have been analyzed: Centralloy® G4852 Micro (designated as GX45NiCrSiNbTi35-25 and called simply G4852 in the following) (Schmidt + Clemens Group, 2009) and stainless steel HK–40 (VanEcho et al., 1967). The former is a high-performance material with excellent resistance to elevated temperatures but comes at a high cost. The latter, while less performant, is more cost-effective. Both materials have been evaluated to determine whether they meet the required performance criteria. For the analyses conducted in this paper, the most critical parameter to consider has been the minimum creep rate (measured in 1/s), which describes the rate of deformation during the secondary creep phase, the longest-lasting stage over time. As a result, the minimum creep rate is the key factor in assessing components subjected to prolonged loading conditions (Sabour, 2013) (pp. 618-629). Table 1 summarizes the mechanical properties of the two materials under investigation.

Table 1. Material properties.

Centralloy® G4852 Micro		
Quantity	Value	Adopted temperature dependence
Density	8.0 g/cm^3	no
Young's modulus @ 20 °C	160 GPa	yes
0.2 % yield strength @ 20 °C	230 MPa	yes
Ultimate tensile strength @20 °C	460 MPa	yes
Elongation at rapture @20 °C	8 %	yes
Thermal conductivity	14.6 W/(mK)	no
Thermal expansion @ 20 °C	$1.555 \cdot 10^{-5}$ 1/K	yes
HK–40		
Quantity	Value	Adopted temperature dependence
Density	8.0 g/cm^3	no
Young's modulus @ 20 °C	161 GPa	yes
0.2 % yield strength @ 20 °C	257 MPa	yes
Ultimate tensile strength @20 °C	471 MPa	yes
Elongation at rapture @20 °C	17 %	yes
Thermal conductivity	14.6 W/(mK)	no
Thermal expansion @ 20 °C	$1.5 \cdot 10^{-5}$ 1/K	yes

Additionally, the dimensional Equation (1) defines the minimum creep rate for G4852, illustrating how high temperatures and elevated stress states accelerate creep deformation:

$$minimum\ creep\ rate = 100 \cdot 60 \cdot 60 \cdot 10^{\left(20-1000 \cdot \frac{-0.00404 \cdot \sigma^3 + 0.18482 \cdot \sigma^2 - 3.04788 \cdot \sigma + 48.74216}{T + 273.15}\right)} \quad (1)$$

where σ is the stress in MPa and T is the temperature in °C. Fig. 1, on the other hand, shows the trend of the minimum creep strain rate as a function of stress and temperature for HK–40 (VanEcho et al., 1967). The exponential increase in creep strain rate with rising stress is particularly evident in Fig. 1, where it is visually emphasized, even though the same effect is described mathematically in Equation (1). This aspect highlights the critical need to design structures that mitigate stress concentrations, which may arise in highly notched areas, contact zones, or constraint regions where individual components are fixed to the structure. This requirement also extends to Finite Element (FE) modelling. A common modeling practice involves simplifying constraints or using rigid elements. However, such simplifications often lead to unrealistically high stress peaks. While these peaks might be dismissed by engineers during post-processing, they can severely jeopardize the accuracy of simulations when creep behavior is introduced. In conclusion, it is important to specify that plasticization has been implemented using the

standard Chaboche's formulation (Chaboche, 2008). However, the tested component has never reached the yield stress, making this setting redundant.

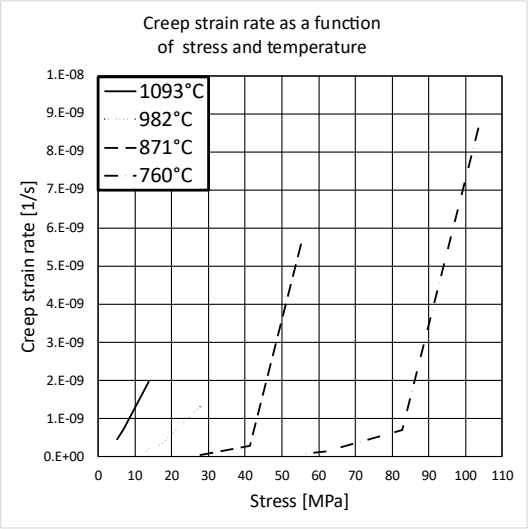

Fig. 1. HK–40: creep strain rate as a function of the stress and of the temperature.

3. Thermal analysis

A thermal analysis has been conducted on a single tube among the many that make up the reactor. The tube presents an inner radius of 70 mm and an external radius of 90 mm and a total length of 19 m. The boundary conditions applied have included a prescribed temperature on the outer surface of the tube and a specific heat flux exiting from the inner wall and entering the fluid contained within it, which, however, has not been explicitly modeled. Fig. 2(a) and 2(b) illustrate the trend of these boundary conditions along the axial coordinate (z in the chosen reference system), as computed through 1D CFD simulations. Although an axisymmetric modeling approach could have been used, a full three-dimensional model has been developed, exploiting one symmetry plane. The 3D modeling has been essential to couple the thermal analysis with the next structural model. A sensitivity analysis has been then performed to determine the necessary element size to accurately capture the stresses, considering that the tube is very thin compared to its axial dimension. Fig. 3(a) provides a detailed view of the mesh used in the analysis. A total of 55'968 hexahedral elements (eight-node, isoparametric, trilinear interpolation function) have been employed for a single tube. The element size has been set to approximately 9 mm along the edges on the surface of the cylinder and approximately 5 mm along the radially distributed edges. Given the total length of the tube of 19 m, using larger elements would have been more efficient. However, the sensitivity analysis highlighted the need for at least two elements through the thickness of the tube, effectively constraining the element size in all dimensions.

Fig. 3(b) and 3(c) present the results of the thermal simulation. It has been enough to perform a single simulation because the two materials have the same thermal conductivity. Fig. 3(b) illustrates the temperature distribution on both the inner and outer surfaces of the tube as a function of the axial coordinate z. Fig. 3(c) depicts the temperature difference between the outer and inner surfaces along the same axial coordinate. This temperature difference has been particularly significant, as it, combined with the relatively minor influence of the axial temperature gradient, has induced differential thermal expansion between the inner and outer surfaces of the tube. This effect generates structural stresses that are particularly detrimental yet unavoidable.

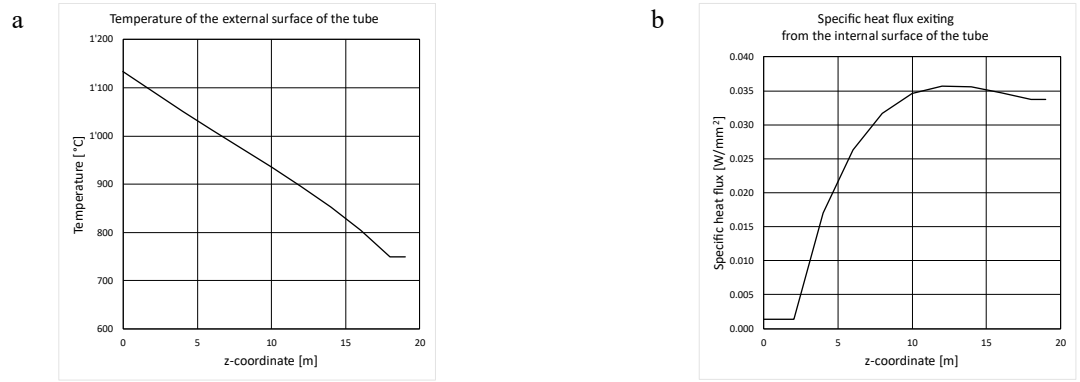

Fig. 2. Thermal boundary conditions: (a) external temperature of the tube; (b) specific heat flux exiting from the internal surface of the tube.

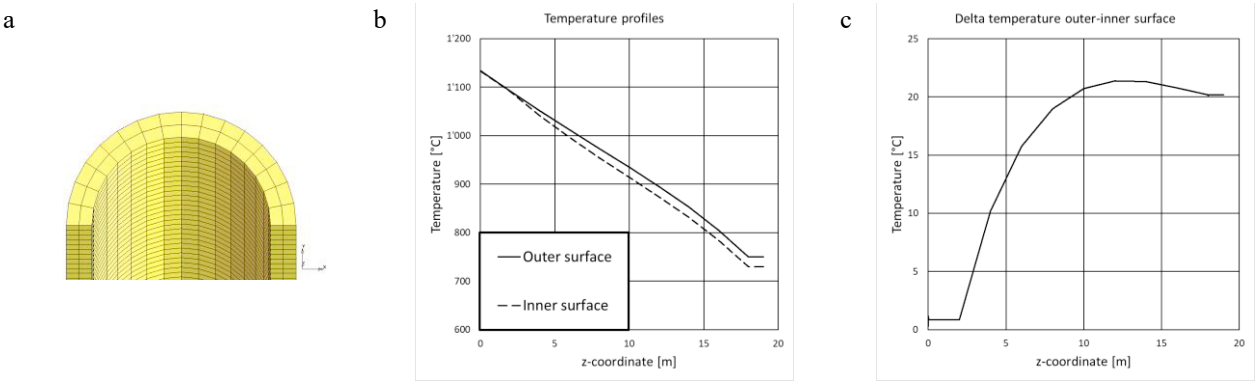

Fig. 3. (a) FE model of the tube; (b) temperature distribution of the outer and inner surface of the tube; (c) difference of temperature between the outer and the inner surface.

4. Thermo-structural analysis

4.1. Base model

The initial thermo-structural analyses have considered the application of three loads. The first has been the thermal load previously calculated. The second has been an internal absolute pressure of 25 bar within the tube. The third has been a tensile load of 3.724 kN to counteract the gravity load associated with the operational scheme of the component under investigation. Fig. 4 provides a simplified schematic of the mounting configuration of the tube. The counterweight, which has the same mass as the tube, has been connected to its upper end and exerts an upward pull from that point. This configuration has been intended to ideally cancel out axial normal stress at the lower joint. The upper section of the tube is particularly critical, as it is exposed to the highest temperatures, is most susceptible to creep, and therefore demands careful consideration in the design process.

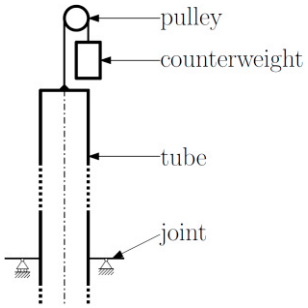

Fig. 4. Schematic of the mounting configuration of the tube.

The first step of the analysis has been to assess the individual contribution of each load without accounting for creep. This evaluation aims at identifying whether any specific loading condition has been particularly critical and, therefore, has required special consideration in the design of the tubular reactor. Table 2 summarizes the maximum von Mises stress recorded across the entire tube for each loading scenario, as well as for the combined case where all three loads have been applied simultaneously. Additionally, the two different materials have been tested to account for variations in their mechanical properties.

Table 2. Maximum values of von Mises stress recorded across the entire tube for each loading scenario.

Loading scenario	von Mises Stress [MPa]	
	G4852	HK–40
Thermal loading	16.5	17.9
Internal pressure	10.3	10.6
Tensile loading	1.5	1.5
Total loading	21.9	22.6

Only minimal differences have been observed in the stress fields. In none of the simulated cases did the materials reach the plastic regime, as both materials exhibit nearly identical mechanical and thermal properties in the linear range. The slightly higher stiffness of G4852 results in marginally lower stress levels.

None of the stress values obtained up to this point have indicated any risk of material failure. The next step has involved considering the phenomenon of creep by incorporating the material properties introduced in Section 2 into the numerical model. Regarding the creep simulations, Table 3 summarizes the results for both materials in terms of maximum von Mises stress, creep strain, and total elongation of the tube after 1’000 hours of operation. When creep behavior has been introduced, the significant differences between the two materials have become evident, clearly highlighting the superior performance of G4852 compared to HK–40. The considerable axial deformation observed under creep conditions requires designers to either implement appropriate expansion joints or mitigate the primary contributing factors, namely, axial stress and elevated temperatures.

Table 3. Results of the simulations including creep.

	G4852	HK–40
Maximum von Mises stress	59.6 MPa	155.7 MPa
Maximum equivalent creep strain	$2.9 \cdot 10^{-3}$	$2.8 \cdot 10^{-2}$
Total axial displacement	280 mm	660 mm

4.2. Effect of the mass of the catalyst material on structural response

The axial stress in the tube is directly influenced by the tensile support system shown in Fig. 4, and therefore by the overall mass of the suspended structure. It is now necessary to assess whether the catalyst material inside the tube, which has not been considered until this point, contributes significantly to the axial load. This catalyst KATALCO 57-4Q (Johnson Matthey, 2019) is introduced in the form of granular particles that fill the entire internal volume. Depending on the assembly configuration, these grains may either rest directly on the bottom of the joint, thus not contributing their weight to the tube, or be partially supported along the length of the tube by internal structures, such as helical inserts or baskets positioned at various axial locations, see the schematic in Fig. 5(a). In this second configuration, the mass of the catalyst is distributed along the length of the tube, leading to a different stress state compared to the previous case. Moreover, radial deformation due to thermal and mechanical loads can cause partial contact with the catalyst grains, even in the absence of intermediate supports. Fig. 5(b) shows that both materials exhibit nearly identical radial displacement trends. Although the actual radial displacement is negligible, it might be useful to refer to the extreme case in which the entire catalyst mass is supported continuously along the tube length, also as a conservative approach to account for potential unforeseen deformations that could cause the catalyst to exert additional loads on the structure. To model this effect, the material density of the tube has been artificially increased to simulate the presence of a distributed additional mass equivalent to that of the catalyst. Table 4 presents the results of these two new numerical simulations. In one case, the stress levels have increased, while in the other they have decreased. This behavior has been caused by the additional tensile load, which shifts the stress state of the elements closer to a hydrostatic condition, typically associated with the state of lower material suffering. It might therefore be concluded that, in this context, the modeling of catalyst support has had a negligible effect on the overall stress distribution.

The next step has been to assess whether this variation in axial stress influences the creep behavior. Table 5 shows that the slight difference in axial loading has not resulted in any noticeable change in creep strain or elongation. Therefore, in the present case study, effective strategies to mitigate creep effects should focus either on reducing operating temperatures or on modifying the geometric design of the tube.

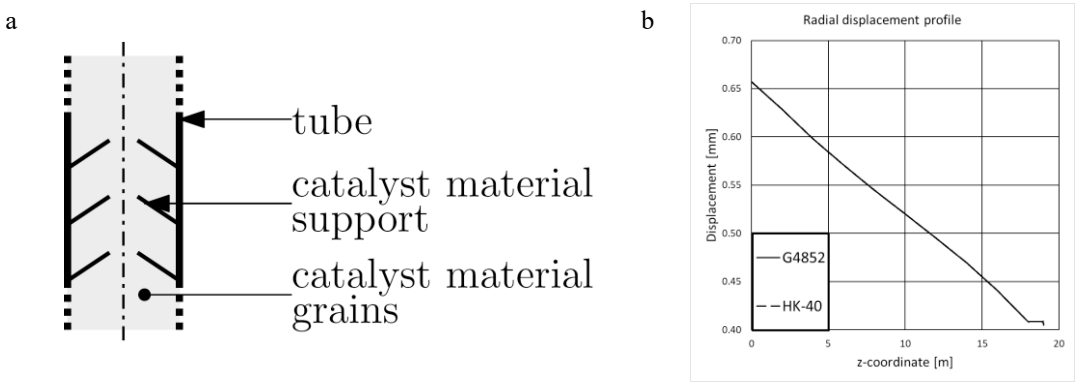

Fig. 5. (a) Schematic of the internal structure to support the catalyst material; (b) trend of the radial displacement along the tube.

Table 4. Maximum value of von Mises stress recorded across the entire tube for the total loading scenario.

Loading scenario	von Mises Stress [MPa]	
	G4852	HK–40
Total loading	21.9	22.1

Table 5. Results of the simulations accounting creep.

	G4852	HK–40
Maximum von Mises stress	59.6 MPa	155.7 MPa
Maximum equivalent creep strain	$2.9 \cdot 10^{-3}$	$2.8 \cdot 10^{-2}$
Total axial displacement	280 mm	660 mm

4.3. Effect of the different mounting strategy

In the final stage of this study, two mounting strategies have been considered. These tubes are typically installed in two rows, all converging into one or more collectors that gather the processed flow, see Fig. 6(a). In the first configuration, the tubes are aligned one behind the other, requiring two separate collectors. In the second configuration, the tubes are coupled in pairs and connected to a single central manifold. In the former case, the tubes experience no additional loading beyond what has been already analyzed. In the latter, however, the mechanical constraint imposed by the manifold restricts their axial expansion, inducing a bending deformation as schematically illustrated in Fig. 6(b), the curvature shown is exaggerated for illustrative purposes. An initial design of the manifold has been incorporated into the numerical model along with appropriate symmetry conditions, as shown in Fig. 6(c). Fig. 7(a) and 7(b) display the resulting deformations, magnified 100 times for clarity. The qualitative deformation has been aligned with the schematic shown in Fig. 6(b). When creep was not considered, both materials have behaved similarly. However, once creep has been included in the simulation, material-specific behavior has become pronounced. Fig. 7(c) and 7(d) present the creep-induced deformations after 1’000 hours of operation, with displacements magnified by a factor of five. The results show that the HK–40 material undergoes significantly greater deformation due to creep, once again confirming the superior performance of the G4852 alloy, albeit more costly, it offers enhanced durability under prolonged thermal and mechanical loading. Table 6 summarizes the quantitative results of these simulations. When creep has not been considered, a significant increase in stress levels has been observed, primarily due to the geometric constraints introduced by the manifold connection. This effect has been especially pronounced in the stiffer G4852 material, which reaches higher stress values compared to HK–40 due to its lower stiffness. Although the overall deformation has been remained limited, these values of stress underscore the importance of carefully addressing manifold geometry during the early stages of design. Under creep conditions, stress and strain levels have remained broadly consistent with those previously observed in Table 3. However, the qualitative deformation patterns differ between configurations and must be considered when selecting the optimal mounting strategy.

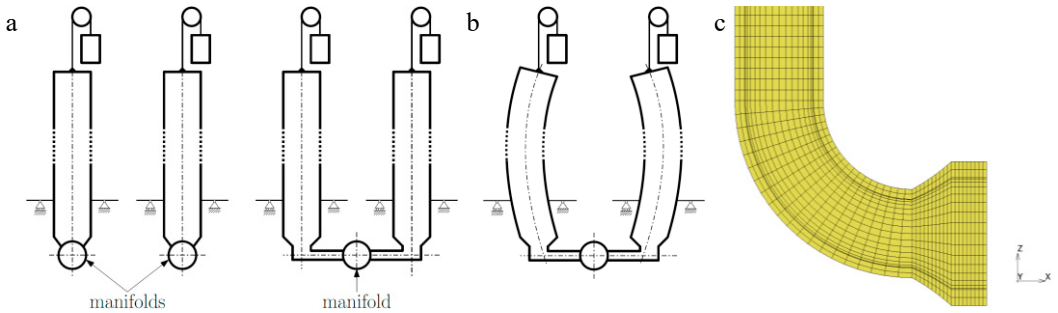

Fig. 6. (a) The two different mounting strategies; (b) qualitative bending deformation; (c) the initial design of the manifold.

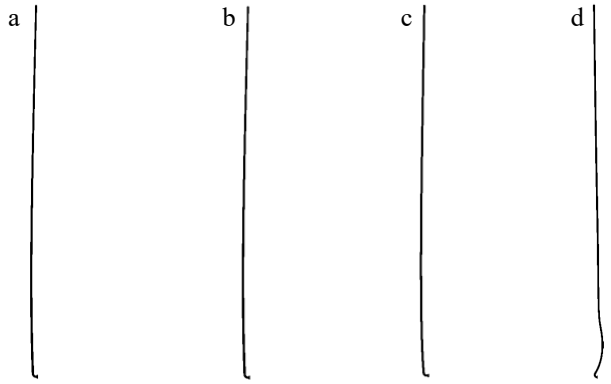

Fig. 7. Deformed shapes of the tubes: (a) G4852 without creep; (b) HK–40 without creep; (c) G4852 with creep; (d) HK–40 with creep.

Table 6. Results of the simulations accounting the central manifold mounting strategy.

	G4852	HK–40
Creep excluded		
Maximum von Mises stress	40.0 MPa	31.1 MPa
Creep included		
Maximum von Mises stress	71.1 MPa	155.7 MPa
Maximum equivalent creep strain	$3.0 \cdot 10^{-3}$	$2.8 \cdot 10^{-2}$
Total axial displacement	284 mm	670 mm

5. Conclusions

The paper has presented a Finite Element methodology for thermo-structural analysis of tubes in a tubular heat exchanger reactor for synthetic fuel production. Two materials were examined in detail: Centralloy® G4852 Micro and HK–40, with particular focus on the creep phenomenon. The research progressed through several phases, beginning with a comprehensive evaluation of material properties, followed by an assessment of various mechanical boundary conditions affecting these tubes. The results demonstrated that without considering creep, both materials exhibited nearly identical responses. However, when creep was included in the analysis, G4852 significantly outperformed HK–40, showing superior resistance to deformation under sustained loading. Further investigation addressed the influence of different support configurations for the catalytic material contained within the tubes. The final phase examined two mounting strategies for connecting tube arrays: individual manifolds for each tube versus a single central manifold. The individual manifold configuration aligned with the calculations performed in the earlier analyses. For the central manifold arrangement, a simplified preliminary design was incorporated into the model. The central manifold configuration substantially increases stress levels when creep is not considered. When creep was included, both configurations appeared quantitatively similar in terms of overall stress and strain values. However, the qualitative deformation patterns differed significantly between the two mounting strategies. Failing to properly account for these deformation patterns during design could compromise the functionality of the entire system. The methodology described and the results obtained have provided valuable insights for the early stages of design when evaluating different materials, boundary conditions, and geometric layouts. This approach may help engineers to make informed decisions regarding material selection, structural configuration, and operational parameters to optimize the performance and longevity of tubular heat exchanger reactors in synthetic fuel production systems.

Acknowledgements

This research project has received funding from the Department of Engineering “Enzo Ferrari”, University of Modena and Reggio Emilia (Italy), under the FARD 2023-2024 program.

References

Awani, K., Hanak, D., Kumar, V., Nabavi, S.A., 2024. Techno-economic assessment of decarbonization pathways for a gas to liquid facility: A review. Journal of CO2 Utilization. https://doi.org/10.1016/j.jcou.2024.102994

Baldino, C., 2023. Provisions for Transport Fuels in the European Union’s finalized “Fit for 55” Package.

Chaboche, J.L., 2008. A review of some plasticity and viscoplasticity constitutive theories. Int J Plast 24, 1642–1693. https://doi.org/10.1016/j.ijplas.2008.03.009

Charkaluk, E., Constantinescu, A., 2000. Energetic approach in thermomechanical fatigue for silicon molybdenum cast iron. Materials at High Temperatures 17, 373–380. https://doi.org/10.1179/mht.2000.17.3.001

Grim, R.G., Ravikumar, D., Tan, E.C.D., Huang, Z., Ferrell, J.R., Resch, M., Li, Z., Mevawala, C., Phillips, S.D., Snowden-Swan, L., Tao, L., Schaidle, J.A., 2022. Electrifying the production of sustainable aviation fuel: the risks, economics, and environmental benefits of emerging pathways including CO_2. Energy Environ Sci 15, 4798–4812. https://doi.org/10.1039/D2EE02439J

Guiducci, A., Barbieri, S.G., Nuzzo, S., Batater, D., Berni, F., Cicalese, G., Fontanesi, S., Franceschini, G., 2023. Refined Structural Design and Thermal Analyses of a High-Speed Wound-Field Generator for the More Electrical Aircraft, in: Proceedings - 2023 IEEE Workshop on Electrical Machines Design, Control and Diagnosis, WEMDCD 2023. Institute of Electrical and Electronics Engineers Inc. https://doi.org/10.1109/WEMDCD55819.2023.10110937

Gupta, P.P., Senthilkumar, S., Kang, S.W., 2022. Study of Gas-to-Liquid Heat Pipe Heat Exchanger. Processes 10. https://doi.org/10.3390/pr10050808

Johnson Matthey, 2019. Steam reforming catalysts [WWW Document]. URL https://matthey.com/documents/161599/348563/JM+Steam+reforming+catalysts+Product+Brochure.pdf (accessed 4.7.25).

Lorenzini, M., Barbieri, S.G., Mangeruga, V., Giacopini, M., 2023. Development of an experimental/numerical validation methodology for the design of exhaust manifolds of high performance internal combustion engines. Eng Fail Anal 152. https://doi.org/10.1016/j.engfailanal.2023.107526

Lorenzini, M., Giacopini, M., Barbieri, S.G., 2018. Thermo-mechanical analysis of the exhaust manifold of a high performance turbocharged engine. Key Eng Mater 774 KEM, 307–312. https://doi.org/10.4028/www.scientific.net/KEM.774.307

Patil, R., Anand, S., 2017. Thermo-structural fatigue analysis of shell and tube type heat exchanger. International Journal of Pressure Vessels and Piping 155, 35–42. https://doi.org/10.1016/j.ijpvp.2017.03.004

Piergiacomi, A., Barbieri, S.G., Mangeruga, V., Giacopini, M., 2025. Influence of Crank Angle Offset on the Mechanical Performance of Different Hydrogen-Fueled Opposed-Piston Engine Architectures. Applied Sciences 15, 2537. https://doi.org/10.3390/app15052537

Ribun, V., Boichenko, S., Kale, U., 2023. Advances in gas-to-liquid technology for environmentally friendly fuel synthesis: Analytical review of world achievements. Energy Reports 9, 5500–5508. https://doi.org/10.1016/j.egyr.2023.04.372

Sabour, M.H., 2013. Creep, in: Wang, Q.J., Chung, Y.-W. (Eds.), Encyclopedia of Tribology. Springer US, Boston, MA, pp. 618–629. https://doi.org/10.1007/978-0-387-92897-5

Schmidt + Clemens Group, 2009. Centralloy® G 4852 Micro, Material data sheet [WWW Document]. URL https://www.schmidt-clemens.com/fileadmin/sc-downloads/werkstoffdatenblaetter/WST_4852_Micro_161109.pdf (accessed 3.11.25).

Shafiee, S., McCay, M.H., 2016. Different reactor and heat exchanger configurations for metal hydride hydrogen storage systems - A review. Int J Hydrogen Energy. https://doi.org/10.1016/j.ijhydene.2016.03.133

Su, X., Zubeck, M., Lasecki, J., Engler-Pinto, C.C., Tang, C., Sehitoglu, H., Allison, J., 2002. Thermal Fatigue Analysis of Cast Aluminum Cylinder Heads, in: Developments in Lightweight Aluminum Alloys for Automotive Applications: 2001-2005. SAE International, pp. 103–109.

TotalEnergies, Airbus, 2024. Airbus and TotalEnergies Sign a Strategic Partnership in Sustainable Aviation Fuels. Paris.

Van Dyk, S., Saddler, J., 2024. Progress in Commercialization of Biojet /Sustainable Aviation Fuels (SAF): Technologies and policies IEA Bioenergy Task 39.

VanEcho, J.A., Roach, D.B., Hall, A.M., 1967. Short-Time Tensile and Long-Time Creep-Rupture Properties of the HK-40 Alloy and Type 310 Stainless Steel at Temperatures to 2000 F. Journal of Basic Engineering 89, 465–478. https://doi.org/10.1115/1.3609640

Wang, B., Ting, Z.J., Zhao, M., 2024. Sustainable aviation fuels: Key opportunities and challenges in lowering carbon emissions for aviation industry. Carbon Capture Science & Technology 13, 100263. https://doi.org/10.1016/j.ccst.2024.100263

Wolft, C., Riefer, D., 2020. Clean Skies for Tomorrow Sustainable Aviation Fuels as a Pathway to Net-Zero Aviation.

Zavattoni, S.A., Good, P., Geissbühler, L., Rutz, D., Toffanin, R., Montorfano, D., Ambrosetti, G., Barbato, M.C., 2024. Performance Evaluation of the Pressurized Synhelion Absorbing Gas Receiver. SolarPACES Conference Proceedings 1. https://doi.org/10.52825/solarpaces.v1i.898

Zavattoni, S.A., Montorfano, D., Good, P., Ambrosetti, G., Barbato, M.C., 2022. Numerical performance evaluation of the Synhelion absorbing gas solar receiver under different operating conditions, in: AIP Conference Proceedings. American Institute of Physics Inc. https://doi.org/10.1063/5.0085733

Zavattoni, S.A., Montorfano, D., Good, P., Ambrosetti, G., Barbato, M.C., 2020. The synhelion absorbing gas solar receiver for 1’500 °C process heat: CFD modeling, in: AIP Conference Proceedings. American Institute of Physics Inc. https://doi.org/10.1063/5.0029314

Zavattoni, S.A., Montorfano, D., Good, P., Geissbühler, L., Rutz, D., Ambrosetti, G., Barbato, M.C., 2023. Synhelion Absorbing Gas Solar Receiver – Design Advancement, in: AIP Conference Proceedings. American Institute of Physics Inc. https://doi.org/10.1063/5.0149049